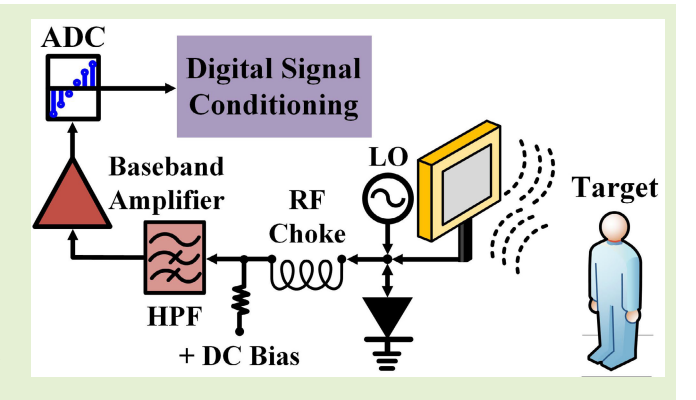


# Quadrature and Single-Channel Low-Cost Monostatic Radar Based on a Novel 2-Port Transceiver Chain

Daniel Rodriguez<sup>®</sup>, *Member, IEEE*, Davi V. Q. Rodrigues<sup>®</sup>, *Member, IEEE*, Ashish Mishra<sup>®</sup>, *Member, IEEE*, Mohammad A. Saed<sup>®</sup>, *Senior Member, IEEE*, and Changzhi Li<sup>®</sup>, *Senior Member, IEEE* 

Abstract—A new radar architecture that features a compact size and only one radio frequency (RF) active device was designed, fabricated, and tested for small motion detection and human range tracking. Unlike conventional board-level radar systems, it contains a single antenna and does not use any low noise amplifier (LNA) or circulator in the RF front end. The I/Q amplitude and phase imbalance present on the system were measured to be <1% and 5.17°, respectively. Besides the local oscillator (LO), there is no other active device consuming dc power. The fabricated radar system has dimensions of  $36 \times 72 \text{ mm} (L \times W)$  and a power consumption of 290 mW in continuous operation. Moreover, a 24-GHz single-channel radar system was designed, fabricated, and tested using the proposed architecture. The dimensions of fabricated board are  $24 \times 27 \text{ mm} (L \times W)$  and total power



consumption of 800 mW dissipated by the LO. The range tracking capabilities of the implemented radar systems were demonstrated by successfully tracking the range of a human target walking back and forth on a hallway. Moreover, the high sensitivity of the proposed quadrature 2-port monostatic Doppler radar was demonstrated by effectively measuring a sinusoidal movement with an amplitude of 2.5  $\mu$ m with a 5.8-GHz carrier.

Index Terms—Doppler radar, frequency-shift keying (FSK), interferometric radar, Internet of Things (IoT), mixer, transceiver.

#### I. INTRODUCTION

DUE to their multipurpose functionality in various applications such as human tracking, vital signs recognition, speech sensing, hand gesture identification, convert weapon detection, structural health monitoring, and traffic safety monitoring [1], [2], [3], [4], [5], [6], [7], [8], [9], [10], [11], [12], [13], [14], [15], [16], [17], radar sensors are under extensive investigation by the scientific community. In the last few years, the interest in low-power and low-cost portable smart sensors

Manuscript received 25 September 2023; accepted 5 October 2023. Date of publication 20 October 2023; date of current version 30 November 2023. This work was supported by the National Science Foundation (NSF) under Grant ECCS-2030094 and Grant ECCS-2112003. The associate editor coordinating the review of this article and approving it for publication was Dr. Wensong Wang. (Corresponding author: Davi V. Q. Rodrigues.)

Daniel Rodriguez is with Intel Corporation, Hillsboro, OR 97124 USA (e-mail: danielfer.rodriguez@gmail.com).

Davi V. Q. Rodrigues is with the Department of Electrical and Computer Engineering, University of Texas at El Paso, El Paso, TX 79968 USA (e-mail: drodrigues@utep.edu).

Ashish Mishra is with Magna International, Cambridge, MA 02138 USA (e-mail: ashishmishra1190@gmail.com).

Mohammad A. Saed and Changzhi Li are with the Department of Electrical and Computer Engineering, Texas Tech University, Lubbock, TX 79409 USA (e-mail: mohammad.saed@ttu.edu; changzhi.li@ttu.edu). Digital Object Identifier 10.1109/JSEN.2023.3324882

has increased to make feasible the massive deployment of sensors demanded in the Internet of Things (IoT) era [18], [18], [20], [21].

The most widely used architecture for low-power and low-cost portable radar sensors is the quadrature direct downconversion architecture, due to its low hardware complexity and easy on-chip integration. However, this architecture uses several active radio frequency (RF) components that increase its power consumption, minimum size, and cost. To tackle this drawback, a simplified direct-conversion microwave front end was proposed in [22]. The local oscillator (LO) power was split between the transmit/receive (TX/RX) antenna and the downconversion mixer by a hybrid coupler. Because the hybrid coupler is a passive 4-port network that is reciprocal, it also split the radar's received signal between the LO and the RF ports of the mixer, resulting in an unwanted 3-dB loss but eliminated the need for expensive components such as a circulator. The total area of the system was 25 cm<sup>2</sup>, including only the microwave circuit and the antenna. Nevertheless, the size of the hybrid coupler is highly dependent on the wavelength of the carrier frequency  $\lambda$ , which limits the minimum size of the system. Afterward, a 2-port monostatic radar that does not use a hybrid or circulator in the RF front end and just exhibits one RF active device was proposed by Rodriguez and Li [23] using a diode-based mixer. The manufactured radar system measures  $20.6 \times 26.5$  mm (length by width) or 5.47 cm<sup>2</sup> in size, excluding the antenna but encompassing a two-stage baseband amplifier. Subsequently, a similar architecture was used in [24] to implement a monolithic microwave integrated circuit (MIMIC) D-band monostatic radar. The system was fabricated in a 130-nm bipolar complementary metaloxide-semiconductor (BiCMOS) technology and includes a compact direct-conversion architecture composed of a diodebased mixer, an oscillator, and an on-chip antenna. However, all these architectures did not support quadrature channels, which jeopardizes the radar's capability of recovering the displacement trajectory and distinguishing between positive and negative Doppler shifts. Moreover, the lack of quadrature channels makes the radar system vulnerable to the well-known null detection point issue, when operating in Doppler mode [25], [26]. In addition, the range tracking capabilities of these compact direct-conversion radars were not studied, limiting the possible applications of these systems.

The microwave techniques described in this article are an extension of the published results elsewhere [23]. In this work, the theoretical analysis and sensing capabilities of the novel, low-cost, low-power 2-port monostatic radar proposed by Rodriguez and Li [23] are expanded. A single-channel radar system is designed and implemented using the 24-GHz industrial, scientific, and medical (ISM) band to verify the scalability of the proposed architecture. The dimensions of the fabricated radar system are  $24 \times 27 \text{ mm} (L \times W)$  or  $6.48 \text{ cm}^2$ taking into consideration the size of a two-stage baseband amplifier but excluding the area occupied by the antenna. Moreover, the range tracking capability of the proposed architecture is verified using frequency-shift keying (FSK) [27], [28], [29], [30]. As a further step, a quadrature 2-port monostatic direct-conversion radar architecture is suggested. Unlike conventional radar systems, this design eliminates the need for separate TX/RX signal chains and uses a single antenna without a hybrid or circulator in the RF front end. Apart from the LO, there is no other RF active device that draws any dc power. A circuit model of the proposed quadrature architecture is developed, showing the diode's location and conversion loss dependence. Moreover, the impact of the mixer's bias point was experimentally studied, for the single- and quadrature-channel systems. This new quadrature architecture is implemented and successfully tested at 5.8 GHz with dimensions of 36  $\times$  72 mm (L  $\times$  W) or 25.92 cm<sup>2</sup>, including a two-stage baseband amplifier for each channel and excluding the area occupied by the antenna.

This article is structured as follows. Section II provides an in-depth analysis of the design principles of the systems. In Section III, the implementation of the radar systems is described, and the measured parameters are compared with the proposed theory. In Section IV, experimental results for human range tracking and small motion detection are presented. Finally, a conclusion is drawn in Section V.

# II. THEORY

# A. Single-Channel System

Prior to delving into the in-depth examination of the hardware design, a concise elucidation of the mixing principle Schottky diode should be maximized; 2) the amount of Authorized licensed use limited to: Texas Tech University. Downloaded on September 11,2024 at 22:48:38 UTC from IEEE Xplore. Restrictions apply.

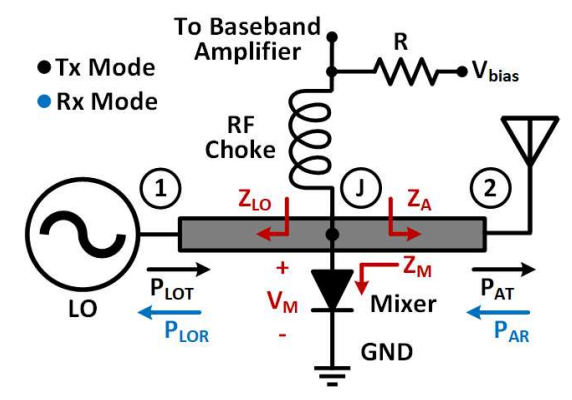


Fig. 1. 2-port transceiver chain schematic.

concerning RF diodes is provided. Suppose that the sum of two microwave signals  $(a_1 \cos(\omega t) + a_2 \cos((\omega + \Delta \omega)t))$ is applied to the input of an RF diode, where  $\omega$  and  $\omega + \Delta \omega$  are carrier frequencies and  $a_1$  and  $a_2$  are realvalued constants. Then, the signal at the diode's output can be written as  $v_o(t) = c_1(\cos(\omega t) + \cos((\omega + \Delta \omega)t)) +$  $c_2(\cos(\omega t) + \cos((\omega + \Delta \omega)t))^2 + \cdots$ , i.e., the first term on the right is the summation of the original two signals, followed by the square of the sum, which can be rewritten as  $(\cos(\omega t) + \cos((\omega + \Delta \omega)t))^2 = \cos(\omega t)^2 + 2\cos(\omega t)\cos((\omega + \Delta \omega)t)^2$  $(\Delta \omega)t + \cos((\omega + \Delta \omega)t)^2$ .  $c_1, c_2, \ldots$  are real-valued constants, and the ellipsis represents all the other higher order powers of the sum that are assumed to be negligible for small signals. By utilizing the trigonometric identity,  $\cos(\omega t)\cos((\omega +$  $(\Delta\omega)t$ ) =  $(\cos(\Delta\omega t) + \cos((2\omega + \Delta\omega)t))/2$ , which demonstrates how the nonlinear effects of a Schottky diode can be leveraged to downconvert the received signals. Even if the higher order powers of the sum were nonnegligible, the resulting output products would lie outside of the baseband frequency band. It is also worth mentioning that an RF choke is used to attenuate higher frequency signals while allowing lower frequency signals to pass through with minimal impedance, so higher order terms will not go into the baseband path (not even the fundamental tone), and the baseband amplifier has a low-pass filter response, which contributes to retrieving a clean signal at the baseband.

Fig. 1 shows the schematic of the implemented single-channel radar system. A 4-port junction along with the diode, the LO, the TX/RX antenna, and the RF choke was created. Since there are only two RF ports in the antenna and LO sections of the configuration, the 4-port junction will be studied as a 2-port transceiver chain. The oscillator is the only microwave component that consumes dc power in the architecture, responsible for the overall power consumption. In addition, the RF choke was used to create an RF isolated port. This port is used to dc bias the mixer and recover the downconverted signal without affecting the RF performance of the system. By changing the dc bias point of the mixer, it is possible to change its effective impedance, which could be used to improve the matching and the conversion loss of the system.

The power division ratio of the 2-port transceiver chain was engineered to maximize radar performance. To enhance the performance of the proposed microwave topology, four conditions must be satisfied: 1) the ac voltage across the Schottky diode should be maximized; 2) the amount of power

received by the antenna that goes into the LO should be minimized; 3) the LO power at the antenna port should be as high as possible without affecting the conversion loss; and 4) a good matching for the two ports should be achieved. To improve the RF power levels across the mixer, it is necessary to consider the transmission line effect. The resultant ac voltage across the diode can be represented as

$$V_M(x_1) = V_0^+ e^{-j\beta x_1} + V_0^- e^{j\beta x_1} \tag{1}$$

where  $V_0^+e^{-j\beta x}$  is the forward propagating voltage,  $V_0^-e^{j\beta x}$ is the backward propagating voltage,  $\beta$  is the phase constant, and  $x_1$  is the position of the diode with respect to port 1. From (1), it can be deduced that the voltage across the diode is highly dependent on its location along the transmission line. Therefore, the location of the mixer must be optimized to achieve the lowest conversion loss. However, if the circuit is well matched (e.g.,  $|V_0^-| \cong 0$ ), the magnitude of the ac voltage across the diode, i.e.,  $|V_M|$ , remains constant at any location on the line, facilitating the design process. To evaluate the second and third conditions, it is necessary to analyze the power flow diagram of the proposed transceiver chain in TX and RX modes, as shown in Fig. 2. The power division ratio in the TX and RX modes can be written as

$$\alpha_T = \frac{P_{\text{AT}}}{P_{\text{MT}}} = \frac{Z_M}{Z_A} \tag{2a}$$

$$\alpha_T = \frac{P_{\text{AT}}}{P_{\text{MT}}} = \frac{Z_M}{Z_A}$$

$$\alpha_R = \frac{P_{\text{LOR}}}{P_{\text{MR}}} = \frac{Z_M}{Z_{\text{LO}}}$$
(2a)

where  $Z_M$ ,  $Z_A$ , and  $Z_{LO}$  are the impedances looking into the mixer, the antenna, and the LO, as shown in Fig. 1, respectively;  $\alpha_T$  and  $\alpha_R$  are the power division ratios in the TX and RX modes, respectively;  $P_{AT}$  and  $P_{MT}$  are the powers going from the LO to the antenna and the mixer in the TX mode, respectively; and  $P_{LOR}$  and  $P_{MR}$  represent the RF power flowing from the antenna to the LO and the mixer, in the RX mode, respectively (refer to Fig. 2). From (2a) and (2b), it can be concluded that the second and third conditions are contradictory to each other (i.e., cannot be satisfied at the same time). For instance, if the TX power  $(P_{AT})$  is increased to satisfy the third condition, the power going from the antenna to the LO  $(P_{LOR})$  will also increase, contradicting the second condition. In addition, the power distribution of the system cannot be arbitrarily changed without affecting the matching at the 2-ports. The reflection coefficient at the LO and antenna ports for a symmetric transceiver chain with a total length of a full wavelength can be written as

$$\Gamma_{LO} = \frac{Z_A Z_0 - Z_M Z_A + Z_0 Z_M}{Z_A Z_0 + Z_M Z_A + Z_0 Z_M}$$

$$\Gamma_A = \frac{Z_0 Z_{LO} + Z_M Z_0 - Z_{LO} Z_M}{Z_0 Z_{LO} + Z_M Z_0 + Z_{LO} Z_M}$$
(3a)

$$\Gamma_A = \frac{Z_0 Z_{LO} + Z_M Z_0 - Z_{LO} Z_M}{Z_0 Z_{LO} + Z_M Z_0 + Z_{LO} Z_M}$$
(3b)

where  $\Gamma_{LO}$  and  $\Gamma_A$  are the reflection coefficients at the LO and antenna ports, respectively. To avoid negatively impacting one of the operation modes, an equal power division ratio was chosen for both, the TX and RX modes (e.g.,  $\alpha_T = \alpha_R = 1$ ). In addition, to have a good matching in the two ports (e.g.,  $\Gamma_{LO} = \Gamma_A \leq -10$  dB) along with a reciprocal structure,  $Z_A$ ,  $Z_{LO}$ , and  $Z_M$  were set to 50  $\Omega$ . Moreover, the total

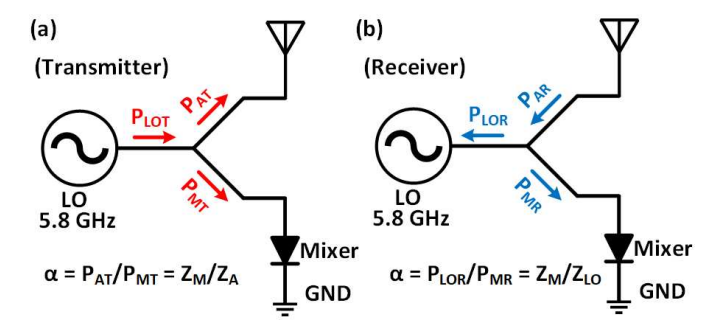


Fig. 2. Graphical representation of the power transfer in a transceiver chain with 2-ports.

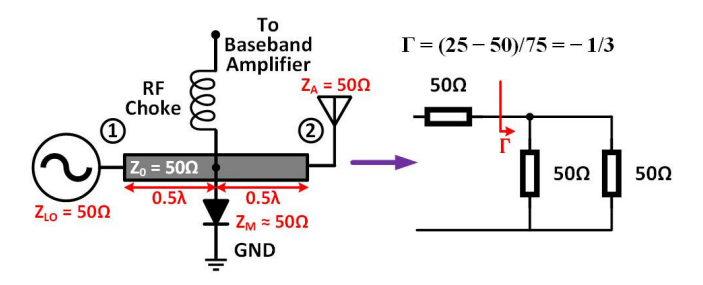


Fig. 3. Proposed system schematic and equivalent circuit.

length of the transceiver chain was set to a full wavelength with the mixer placed at a half-wavelength distance from each port. Fig. 3 shows the schematic and equivalent circuit of the proposed system. It is important to note that the impact of the mixer's location is reduced since a good matching is expected on the system.

# B. Quadrature-Channel System

To incorporate a quadrature channel in the proposed 2-port transceiver chain, it is necessary to add an ac-coupled but dcisolated structure to the proposed system. In other words, the LO signal must be shared between the mixers of each channel, but the generated IF signals should be isolated. Otherwise, they will mix together. The proposed architecture is shown in Fig. 4, a capacitor was used to isolate the downconverted quadrature baseband signals, and a quarter-wave transformer was added in series with the RF choke to improve the isolation of the isolated port. The improved isolation is necessary to avoid adding additional phase shifts to the RF and LO signals due to the baseband circuit components. To generate the two quadrature signals, it is necessary to introduce a 90° phase shift between the two channels. To produce the desired phase shift without adding any additional microwave structure, the two Schottky diodes are placed  $2\pi n + \pi/4$  degrees apart from each other. As the signal travels twice through the 2-port transceiver chain (e.g., in TX and RX modes), the total phase shift applied due to the distance between the mixers is equal to 90° (e.g.,  $\pi/2$ ), which generates the quadrature channels. Fig. 4 shows the quadrature-channel generation. For simplicity, just the LO's incident propagating wave was used for illustration. The LO signal can be modeled as  $cos(\omega t)$ , after traveling through  $L_1$  and reaching the junction J, the LO signal can now be represented as  $\cos(\omega t - \phi_1)$ , where  $\phi_1$  is the phase shift due to  $L_1$ . When the signal reaches junction  $J_1$ , an additional

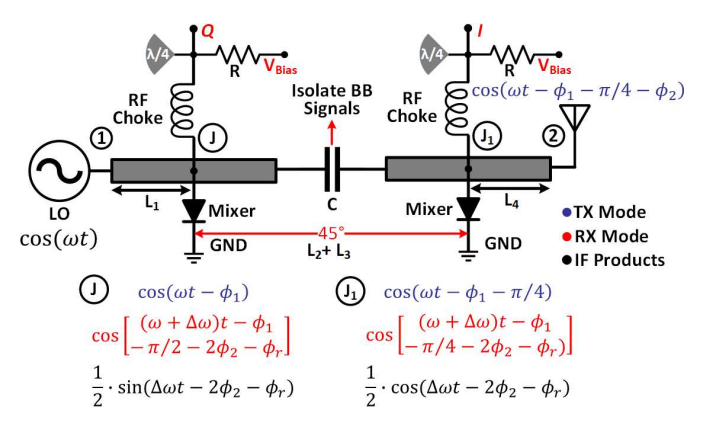


Fig. 4. Proposed quadrature direct-conversion architecture.

45° phase shift will be applied, and this additional phase shift can be represented as  $\cos(\omega t - \phi_1 - \pi/4)$ . Then, after traveling through  $L_4$ , the signal will be radiated by the antenna, the TX signal can be modeled as  $\cos(\omega t - \phi_1 - \pi/4 - \phi_2)$ , where  $\phi_2$ is the phase shift applied by  $L_4$  to the signal. The reflected RF signal at  $J_1$  can be represented as  $\cos[(\omega + \Delta \omega)t - \phi_1 \pi/4 - 2\phi_2 - \phi_r$ ), where  $\Delta \omega$  is the Doppler shift applied by the target to the signal and  $\phi_r$  is the phase delay due to the distance between the target and the radar. When the reflected RF signal travels from  $J_1$  to J, an additional 45° phase shift is applied. Therefore, the reflected RF signal at the junction J can be represented as  $\cos[(\omega + \Delta\omega)t - \phi_1 - \pi/2 - 2\phi_2 - \phi_r)]$ . As can be seen, the TX/RX signals at junction J are 90° out of phase, and thus, the generated IF products at each junction by the mixers can be modeled as  $0.5 \cdot \sin(\Delta \omega t - 2\phi_2 - \phi_r)$  and  $0.5 \cdot \cos(\Delta \omega t - 2\phi_2 - \phi_r)$ , showing the effectiveness of the proposed architecture to generate quadrature baseband signals.

A circuit model of the proposed architecture was developed as shown in Fig. 5, the capacitor C was modeled as a short circuit for the RF, and the added phase shift was included in  $L_2 + L_3$ . From Fig. 5, the voltage at  $D_1$  due to LO can be modeled as

$$v_{d_1}^o = \frac{Z_{\text{eq}_1}^o Z_{\text{in}}^o}{\left(Z_{\text{in}}^o + Z_s\right) \left(Z_{\text{eq}_1}^o A_1 + B_1\right)} v_{\text{LO}} \tag{4}$$

where  $Z_{\text{eq}_1}^o = Z_{x_1}^o \parallel Z_{d_1}$ ,  $Z_{d_1}$  is the  $D_1$  equivalent impedance,  $A_1 = \cos(\beta L_1)$ , and  $B_1 = j Z_0 \sin(\beta L_1)$ . Following the same analysis, the voltage at  $D_2$  due to the LO can be modeled as follows:

$$v_{d_2}^o = \frac{Z_{\text{eq}_2}^o Z_{\text{in}}^o}{\left(Z_{\text{in}}^o + Z_s\right) \left(Z_{\text{eq}_2}^o A_{\text{eq}_1} + B_{\text{eq}_1}\right)} v_{\text{LO}}$$
 (5)

where  $A_{\rm eq_1}$  and  $B_{\rm eq_1}$  come from the ABCD parameters of the line  $L_1$ , the diode  $D_1$ , and the line  $L_2+L_3$ ,  $Z_{\rm eq_2}^o=Z_{X_2}^o\parallel Z_{d_2}$ , and  $Z_{d_2}$  is the  $D_2$  equivalent impedance. To calculate the generated IF, it is necessary to calculate both the LO and the RF received signal contributions to the voltage across the diodes. Therefore, the voltage in  $D_2$  due to the RF received signal is given by

$$v_{d_2}^r = \frac{Z_{\text{eq}_1}^r Z_{\text{in}}^r}{\left(Z_{\text{in}}^r + Z_a\right) \left(Z_{\text{eq}}^r A_4 + B_4\right)} v_{\text{RF}}$$
 (6)

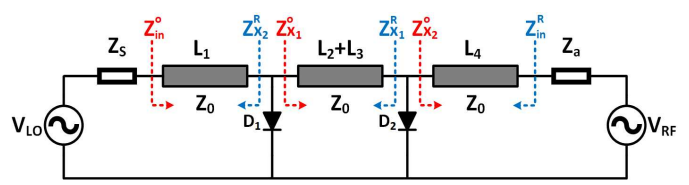


Fig. 5. Quadrature 2-port transceiver chain equivalent circuit.

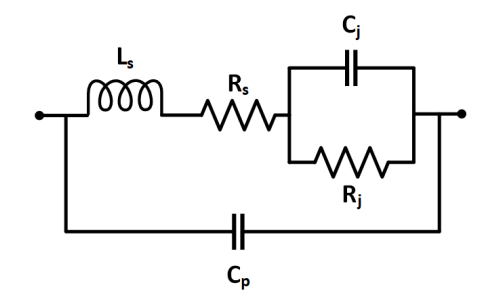


Fig. 6. RF equivalent circuit model of a Schottky diode.

where  $Z_{\text{eq}_1}^r = Z_{X_1}^r \parallel Z_{d_2}$ ,  $A_4 = \cos(\beta L_4)$ ,  $B_4 = j Z_0 \sin(\beta L_4)$ , and  $v_{\text{RF}}$  is the RF received signal. Likewise, the voltage in  $D_1$  due to the RF received signal can be modeled as

$$V_{d_1}^r = \frac{Z_{\text{eq}_2}^r Z_{\text{in}}^r}{\left(Z_{\text{in}}^r + Z_a\right) \left(Z_{\text{eq}_2}^r A_{\text{eq}_2} + B_{\text{eq}_2}\right)} v_{\text{RF}} \tag{7}$$

where  $Z_{\text{eq}_2}^r = Z_{X_2} \parallel Z_{d_1}$  and  $A_{\text{eq}_2}$  and  $B_{\text{eq}_2}$  come from the ABCD parameters of the line  $L_4$ , the diode  $D_2$ , and the line  $L_2 + L_3$ . As can be seen, the ac voltage across the diodes depends on the lengths of  $L_1$  and  $L_4$ , and thus, their lengths cannot be arbitrarily chosen.

To complete the model, it is necessary to estimate the impedance of the Schottky diodes. For this purpose, the circuit model shown in Fig. 6 was adopted, where  $R_j$  is the junction resistance of the diode,  $C_j$  is the junction capacitance,  $R_S$  is the bulk resistance, and  $L_S$  and  $C_p$  are the packaging inductance and capacitance, respectively [31]. From Fig. 6, the admittance of the Schottky diode can be written as follows:

$$Y_d = \left(R_s + j\omega L_s + \frac{R_j \frac{1}{\omega C_j}}{\frac{1}{\omega C_j} + jR_j}\right)^{-1} + j\omega C_p.$$
 (8)

The nonlinear behavior of a Schottky diode comes from the junction capacitance and resistance  $C_j$  and  $R_j$ . The nonlinear junction capacitance can be modeled as shown in (9), where Q is the charge stored in the diode's junction and  $V_j$  is the voltage across the junction

$$C_j = \frac{\partial Q}{\partial V_i}. (9)$$

The overall nonlinear junction resistance is given by (10), where  $\eta_0$  is the diode ideality factor,  $I_S$  is the reverse saturation current, and  $I_{SD}$  is the voltage-controlled current through the Schottky diode junction

$$R_j = \left(\frac{\partial I}{\partial V_j}\right)^{-1} = \frac{\eta_0 V_T}{I_S + I_{SD}}.$$
 (10)

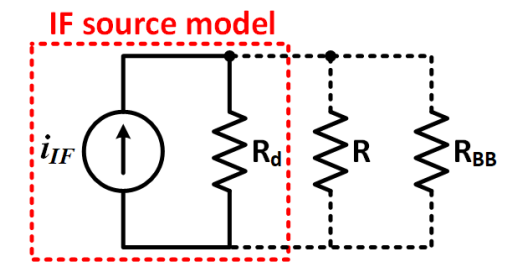


Fig. 7. Schottky diode IF source model.

The total IF current generated in the proposed quadrature direct-conversion architecture can be calculated at each mixer as

$$i_{\rm IF_1} = \frac{1}{2} G'_d V^r_{d_1} V^o_{d_1} \tag{11a}$$

$$i_{\text{IF}_2} = \frac{1}{2} G'_d V'_{d_2} V'_{d_2}$$
 (11b)

where  $G'_d = (G_d/V_T)$ ,  $G_d = (1/R_j)$  is called the dynamic conductance of the diode,  $V_T \approx 25$  mV is the thermal voltage, and  $i_{\rm IF_1}$  and  $i_{\rm IF_2}$  are the generated IF currents by  $D_1$  and  $D_2$ , respectively.

# C. Other Considerations

In small-signal low-frequency analysis, the bias resistor R is in parallel with the Schottky diode and the baseband amplifier input resistance. Therefore, its impact on the conversion loss and the noise performance of the system must be analyzed. The circuit model of a Schottky diode as an IF source is shown in Fig. 7, where  $R_d$  is the diode intrinsic resistance and  $i_{\rm IF}$  can be modeled by (11). From Fig. 7, it can be deduced that if the value of R and the baseband amplifier input resistance  $R_{\rm BB}$  are high compared with  $R_d$ , the total equivalent resistance seen by  $i_{\rm IF}$  will be  $R_d \parallel R \parallel R_{\rm BB} \approx R_d$ . Therefore, the conditions of  $R \gg R_d$  and  $R_{\rm BB} \gg R_d$  must be satisfied to avoid loading the mixer and negatively impacting the conversion loss of the system.

In addition, to optimize the system performance, it is necessary to assess the noise contribution of the bias resistor R to the recovered baseband signal. To perform this analysis, it is necessary to use the equivalent circuit for noise analysis of the implemented baseband amplifier, as shown in Fig. 8 [32]. Any noisy resistor can be modeled as a noiseless resistor in parallel with a noise current source or its corresponding Thevenin equivalence [32]. The thermal noise current variance per hertz of bandwidth generated by any generic resistor  $R_x$  can be modeled as  $i_{Rx}^2 = 4 \text{ kT}/R_x$ , where k is Boltzmann's constant in joules per kelvin, T is the resistor's absolute temperature in kelvins, and  $R_x$  is the resistor value in ohms [32]. The noise of an operational amplifier (op amp) is characterized by three equivalent noise sources: two current sources with spectral densities  $i_{nn}$  and  $i_{np}$ , and a voltage source with spectral density  $e_n$  [32]. A practical op amp can be modeled as a noiseless op amp fed with these three sources at the input, as shown in Fig. 8. The superposition principle was applied to calculate the overall noise spectral density  $e_{ni}$  referred to the input of the op amp. However, the induvial terms must be added in a

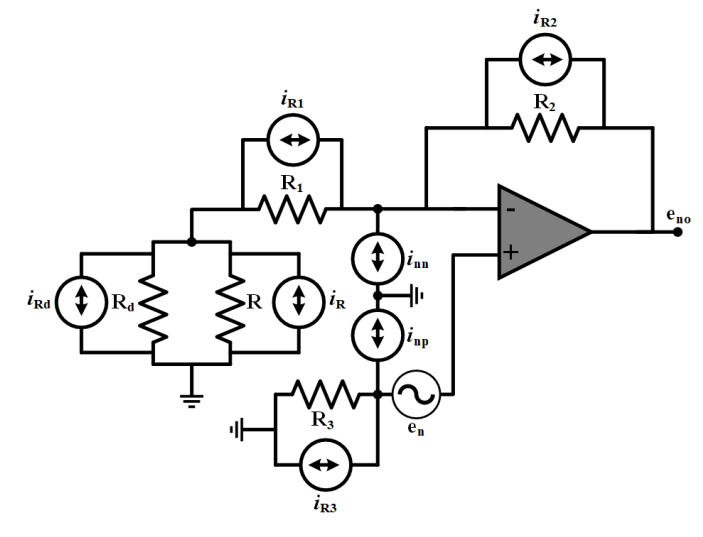


Fig. 8. Equivalent circuit for noise analysis of the implemented baseband amplifier.

power fashion. From Fig. 8, the overall input-referred noise power spectral density for the amplifier can be modeled as

$$e_{\text{ni}}^{2} = e_{n}^{2} + 4kT \begin{pmatrix} R_{3} + \frac{R_{2}(R_{1} + R_{\text{eq}})^{2} + R_{1}R_{2}^{2}}{(R_{1} + R_{2} + R_{\text{eq}})^{2}} \\ + \frac{(R_{\text{eq}} \parallel (R_{1} + R_{2}))^{2}}{R_{\text{eq}}} \end{pmatrix} + R_{3}^{2}i_{\text{np}}^{2} + (R_{2} \parallel (R_{1} + R_{\text{eq}}))^{2}i_{\text{nn}}^{2}$$
(12)

where  $R_{\rm eq} = R_d R/(R_d + R)$  is the parallel combination of  $R_d$  and R. For ac-coupled interferometric radars, the value of  $R_1$  is usually in hundreds of kiloohms to obtain the necessary low cutoff frequency to remove the dc component while passing the low frequencies generated by slow motions (e.g., respiration and heartbeat) [33], [34], [35], [36], [37]. From (12), it can be deduced that to reduce the noise contribution of R and  $R_d$  to the system, it is necessary to satisfy the condition of  $R_1 \gg R_d$ . If this condition is satisfied,  $R_1$  will be much bigger than  $R_{\rm eq}$  and (12) can be rewritten as shown in (13), where the negligible effect of R and  $R_d$  on the total input-referred noise power spectral density of system is evidenced

$$e_{\text{ni}}^2 = e_n^2 + 4kT[R_3 + (R_1 \parallel R_2)] + R_3^2 i_{\text{np}}^2 + (R_2 \parallel R_1)^2 i_{\text{nn}}^2.$$
 (13)

# III. SYSTEM IMPLEMENTATION AND ELECTRONIC CHARACTERIZATION

#### A. Single-Channel System

To verify the scalability of the proposed system to higher frequencies as compared with [23], a 24-GHz 2-port single-channel monostatic radar was implemented, as shown in Fig. 9. A 125- $\mu$ m Rogers Duroid 5880 substrate was used to fabricate the radar system. The RF choke was implemented using a radial stub and a quarter wavelength transmission line since RF structures have a small size at millimeter-wave frequencies and lumped elements usually exhibit lower self-resonant frequencies. The nonlinear detector (mixer) was built using the Skyworks SMS7621-040LF Schottky diode.

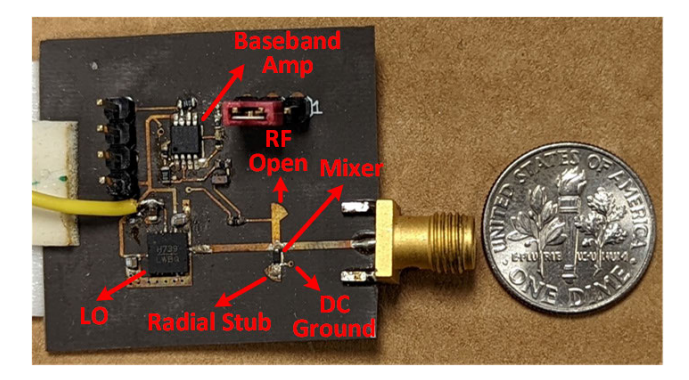


Fig. 9. Fabricated 24-GHz radar system.

A quarter wavelength radial stub with a shunt dc line was leveraged to provide a dc and ac ground to the cathode of the diode. The LO (Analog Devices HMC739LP4) has a power consumption of 800 mW, which is the total power consumption of the RF front end. An output power reading of 8 dBm was obtained through measurement, which matches with the manufacturer specification. A two-stage noninverting amplifier was developed for the baseband circuit. An RC highpass filter was employed to remove the dc component. The cutoff frequency of the high-pass filter is 0.16 Hz since R =100 k $\Omega$  and  $C = 10 \mu F$ . On the other hand, the minimum detectable frequency is a function of several relevant factors such as the strength of the received signals, the conversion loss, and the baseband filter attenuation at that frequency. The designed sensor has dimensions of 24  $\times$  27 mm (L  $\times$  W) or 6.48 cm<sup>2</sup> without the antenna but including a two-stage baseband amplifier. An SMA connector was placed on the antenna port to interface with a commercial horn antenna.  $S_{11}$  for the 24-GHz horn antenna (WR-42 waveguide standard gain horn antenna by Pasternack) was measured as -25 dB at 24GHz.

An additional 2-port RF transceiver without the LO was constructed to evaluate the performance of the designed structure. The S-parameters were calculated for different values of  $V_{\text{bias}}$ , using a bias resistor  $R = 2.3 \text{ k}\Omega$ . The measured S-parameters are shown in Fig. 10. As can be seen, when the bias voltage increases, the matching improves, but the TX power slightly reduces. To assess the impact of  $V_{\rm bias}$  on a system level, the conversion loss for different bias voltages was measured and the obtained results are shown in Fig. 11. The conversion loss of the system was measured by feeding an 8-dBm 24-GHz signal into the LO port and a −14-dBm RF signal with a 1-kHz offset into the antenna port. As shown in Fig. 11, the variation in the conversion loss is less than 2 dB when the bias voltage is swept from 0 to 5 V. It is important to notice that the impact of this variation to the radar's performance is even smaller than 2 dB since these measurements do not account for the reduction in TX power. As a result,  $V_{\text{bias}} = 0 \text{ V}$  was selected in this work since the conversion loss improvement does not compensate for the increased power consumption and hardware complexity. In addition, for  $V_{\text{bias}} = 0 \text{ V}$ ,  $S_{11}$  and  $S_{22}$  are below -10 dB, which pushes  $S_{21} \cong S_{12}$  above -3 dB, verifying the authors' analysis for the single-channel system.

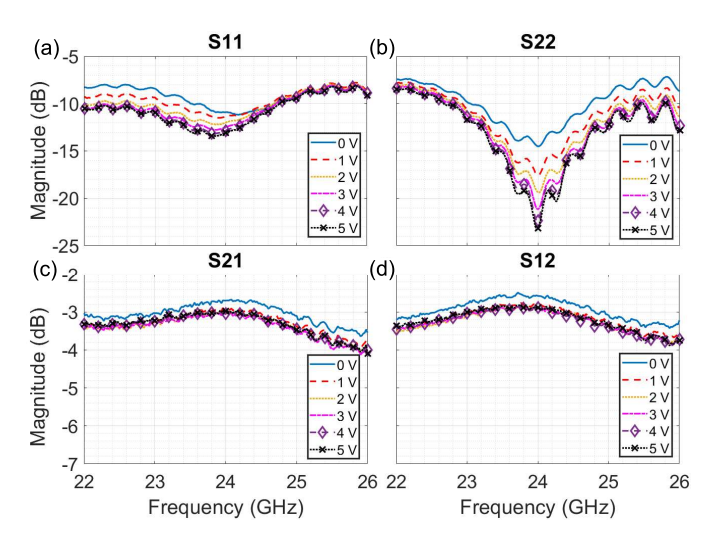


Fig. 10. Measured (a)  $S_{11}$ , (b)  $S_{22}$ , (c)  $S_{21}$ , and (d)  $S_{12}$  for different bias voltages for the fabricated 24-GHz radar system.

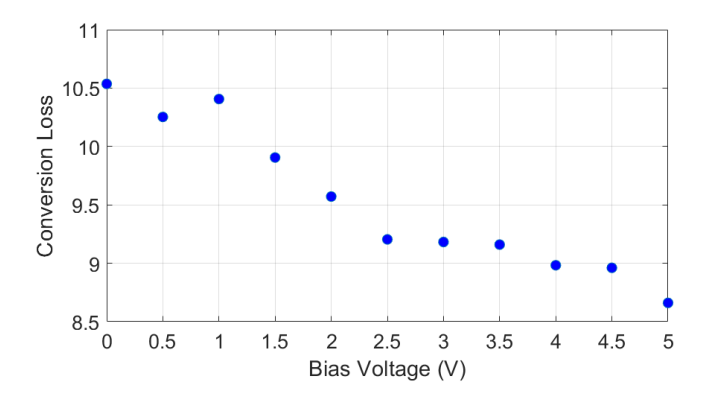


Fig. 11. Measured conversion loss for different values of  $V_{\rm bias}$ .

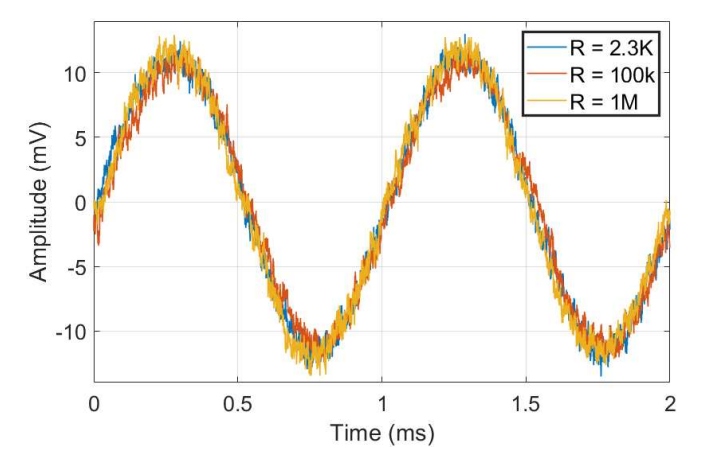


Fig. 12. Measured baseband signal for different values of R.

To verify the negligible effect of the dc bias resistor R on the system's conversion loss (e.g.,  $R\gg R_d$ ), the conversion loss was measured for R equal to 2.3, 100, and 1000 k $\Omega$ . For these experiments, the value of  $V_{\rm bias}$  was set to 0 V, to avoid changes on the bias point of the diode. The recovered baseband signals for each value of R are shown in Fig. 12. As can be seen, the recovered signals have almost identical amplitudes and noise performance, verifying the authors' theoretical analysis.

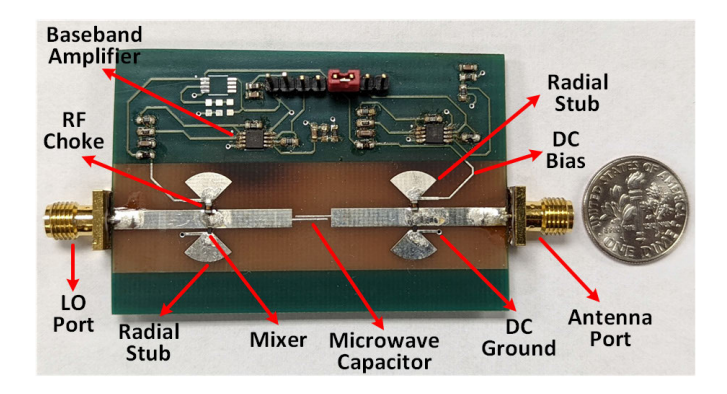


Fig. 13. Fabricated characterization board for the 5.8-GHz quadrature radar system.

# B. Quadrature-Channel System

A 5.8-GHz quadrature 2-port monostatic radar system was implemented, as shown in Fig. 13. A low-cost 1.57-mm-thick FR4 substrate was utilized to design the entire system. With the LO (Analog Devices HMC358MS8G) being the sole active RF component in the proposed design, the power consumption of the 2-port quadrature monostatic front end is constrained to 290 mW. The I/Q mixers were designed and implemented using the Infineon BAT15-02L Schottky diode. The provision of ac and dc ground to the cathode of each diode was accomplished using a shunt dc line and a 90° radial stub. In addition, a 90° radial stub with a shunt line was added to each isolated port to improve the isolation. These shunt lines were used to recover the quadrature baseband signals and provide dc bias to the diodes. The lengths of  $L_1$  and  $L_4$  were optimized in simulation to achieve the minimum conversion loss ( $L_1 = L_4 \approx 0.53\pi$ ). A two-stage noninverting amplifier was specifically created for the baseband circuit. To simplify the amplifier design, an RC high-pass filter was utilized to separate the dc component. The designed RF transceiver has dimensions of 36  $\times$  72 mm ( $L \times W$ ) or 25.92 cm<sup>2</sup>, including the area occupied by the two-stage baseband amplifier for each channel and excluding the area occupied by the antenna. As shown in Fig. 13, a microstrip interdigital capacitor (MICAP) was designed and implemented to isolate the generated quadrature signals. The simulated and measured S-parameters of the MICAP are shown in Fig. 14. As can be seen, the simulated and measured results are in good agreement.  $S_{11}$  and  $S_{21}$  at 5.8-GHz were measured as -23.2 and -1.23 dB, respectively. Therefore, the implemented MICAP exhibits good matching and low loss while successfully isolating the quadrature baseband signals. The 5.8-GHz patch antenna was designed with the FR4 substrate.  $S_{11}$  of the antenna was measured as -9.42 dB at 5.8 GHz.

The S-parameters of the implemented 5.8-GHz 2-port quadrature monostatic radar system were measured for different values of  $V_{\rm bias}$ , using a bias resistor  $R=2.3~{\rm k}\Omega$ . The measured S-parameters are shown in Fig. 15. As can be seen, when the bias voltage increases, the matching remains constant, but  $S_{21}$  and  $S_{12}$  of the system decrease (e.g., higher insertion loss). It is important to notice that a higher insertion loss reduces the total TX power, negatively impacting the radar

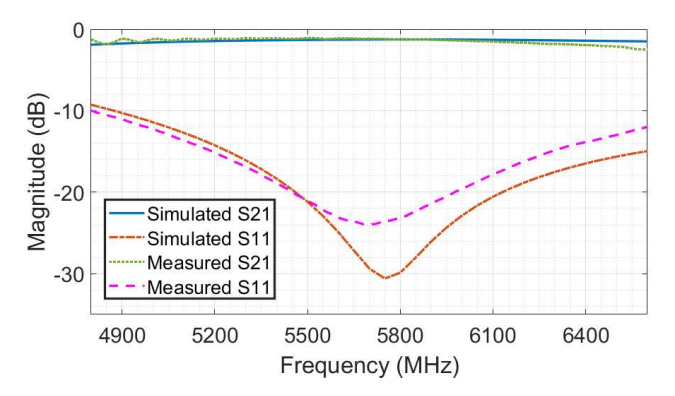


Fig. 14. Measured and simulated S-parameters of the MICAP.

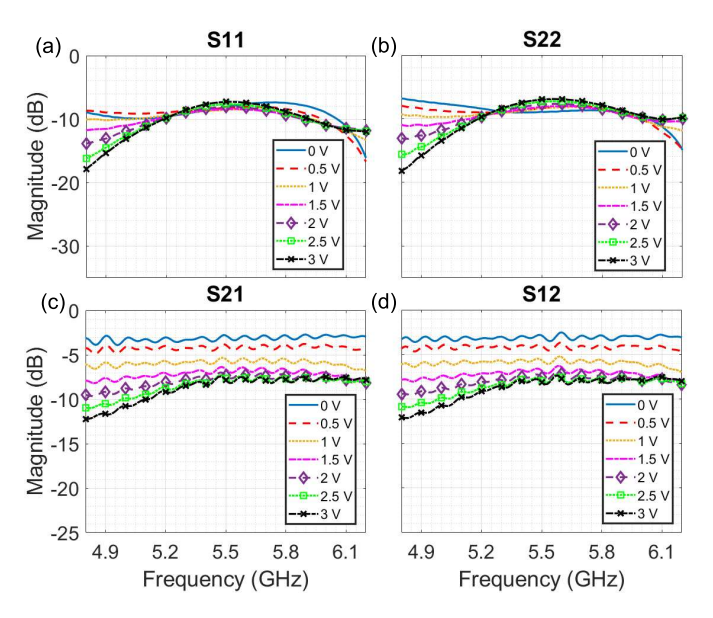


Fig. 15. Measured (a)  $S_{11}$ , (b)  $S_{22}$ , (c)  $S_{21}$ , and (d)  $S_{12}$  of the fabricated 5.8-GHz quadrature radar system.

TABLE I
PERFORMANCE CONVERSION LOSS FOR DIFFERENT VALUES OF R

R (kΩ)	$R = 2.3k\Omega$	$R = 100 k\Omega$	$R = 1M\Omega$
$CL_{I}(dB)$	6.9	6.7	6.6
$CL_{Q}(dB)$	6.4	6.2	6.0

LO = 10 dBm, RF = -30 dBm, 1 kHz offset,  $V_{bias} = 0 \text{ V}$ 

TABLE II

PERFORMANCE CONVERSION LOSS FOR DIFFERENT VALUES OF  $V_{\mathsf{BIAS}}$ 

V <sub>bias</sub> (V)	0.5	1	1.5	2	2.5	3
CL <sub>I</sub> (dB)	6.68	6.68	6.89	6.47	6.89	6.89
$CL_Q$ (dB)	6.26	6.26	6.47	6.06	6.06	6.26

LO = 10 dBm, RF = -30 dBm, 1 kHz offset,  $R = 2.3 \text{k}\Omega$ 

performance. Therefore,  $V_{\rm bias} = 0$  V was chosen as the optimal operating point. Different values of R and  $V_{\rm bias}$  were used to evaluate the conversion loss of the system. The obtained results are shown in Tables I and II.

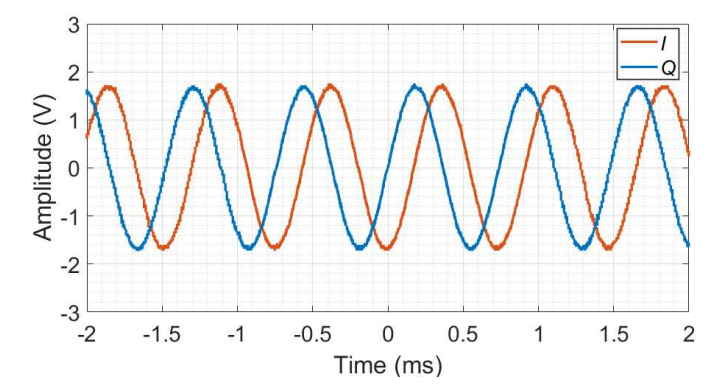


Fig. 16. Measured quadrature baseband signals.

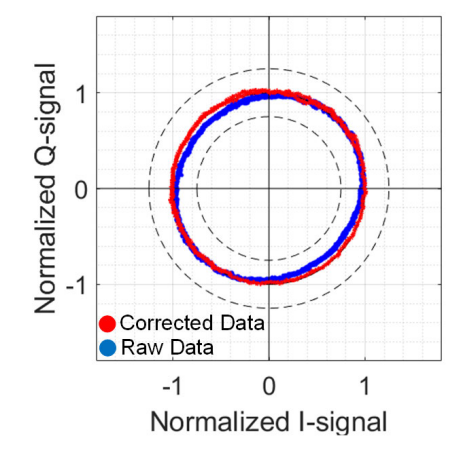


Fig. 17. Constellation plot of the measured and corrected quadrature baseband signals.

To verify the orthogonality of the generated I/O channels, two signals with a 1.4-kHz offset were fed into the LO and antenna ports. A circulator was placed at each port to reduce the interaction between the signal generators. The recovered baseband signals are shown in Fig. 16. The measured amplitude error between the signals is below 1% and the measured phase difference between the two channels is  $84.83^{\circ}$ . To illustrate the I/Q distortion present on the system, the constellation plot of the recovered quadrature signals was computed, to compare it with the trajectory that fits the unitary circle. In addition, a distortion correction method was applied to the recovered signal. As shown in Fig. 17, the recovered I/Q channels are almost balanced and the constellation plot closely overlaps with the trajectory that fits the unitary circle. Moreover, the correction method was enough to offset the distortion, mitigating the small imbalance present in the system. It should be noted that different diode biases may not significantly affect the I/O amplitude and phase imbalances since the designed structure functions as a quasi-reciprocal 2-port network.

# IV. SYSTEM EXPERIMENTAL RESULTS A. Single Human Tracking

FSK modulation was used to perform range measurements with the implemented radar systems. A radar system that utilizes FSK transmits two distinct frequencies,  $f_1$  and  $f_2$ ,, through a common RF chain at a switching rate of  $f_{SGT}$ .



Fig. 18. Human range tracking experimental setup.

If a target moves at a constant velocity, the reflected signal undergoes a frequency shift due to the Doppler effect, which can be used to track its range. In addition, a phase delay will also be applied to the signal, due to its round-trip travel. Therefore, by comparing the phase of the two downconverted tones, the instantaneous distance between the target and the FSK radar can be estimated as  $R_0 = c\Delta\phi(t)/4\pi\Delta f$ , where c is the speed of light,  $\Delta\phi(t)$  is the time-varying phase different of the two downconverted tones, and  $\Delta f$  is the frequency difference of the transmitted discrete tones. As the phase of a sine signal repeats every  $2\pi$ , the maximum unambiguous range of an FSK quadrature system is limited to  $R_{\rm max} = c/2\Delta f$ . It is important to notice that, as shown in [38] and [39], the maximum unambiguous range for single-channel radar system is reduced by half compared to quadrature systems.

For the single human tracking experiments, all the implemented radar systems were used, including the 5.8-GHz single-channel system introduced in [23]. The frequency difference between the two carrier signals for all the experiments was set to  $\Delta f = 8.8$  MHz. Therefore, the maximum unambiguous range can be approximated as 17 m for a quadrature system and 8.5 m for a single-channel system. To avoid the antenna nearfield and limit the experiment within the maximum unambiguous range for the single-channel radar systems, a human subject was asked to complete a round trip from 2 to 8 m with a normal walking speed, as shown in Fig. 18. The recorded data were measured with a 15-kHz sampling frequency. A Hamming window and zero padding were utilized in conjunction with a 0.2-s window length for the fast Fourier transform (FFT). Information about the Doppler frequencies generated by the waking human can be derived after an analysis of both spectra. Then, by analyzing the phase difference between the two Doppler frequencies, the subject's instantaneous range can be estimated. The experimental results obtained using the implemented single-channel systems are shown in Fig. 19, which confirms the range tracking capabilities of the proposed architecture.

To exploit the extended range capabilities of quadrature radar systems and assess the performance of the implemented

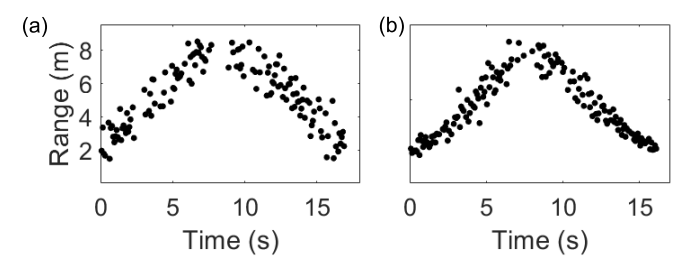


Fig. 19. Range tracking results obtained for a person walking in an interior corridor, moving back and forth between 2 and 8 m, using (a) 5.8- and (b) 24-GHz single-channel systems.

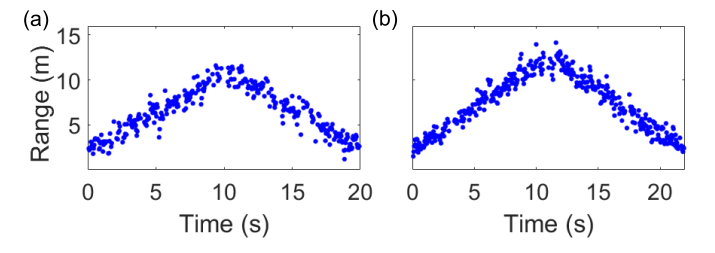


Fig. 20. Range tracking results obtained for a person walking in an interior corridor walking back and forth between (a) 2 and 11 m and (b) 2 and 13 m using the 5.8-GHz quadrature-channel system.

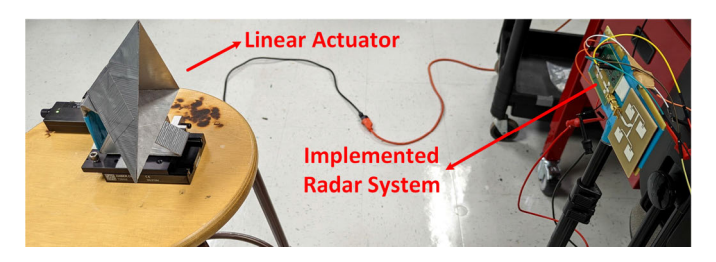


Fig. 21. Experimental setup for small motion detection using the proposed quadrature 2-port monostatic system.

2-port monostatic quadrature-channel system, the subject was asked to complete two different round trips, one from 2 to 11 m and the other one from 2 to 13 m, walking at normal speed. The experimental results are shown in Fig. 20, where the range of the human target was successfully recovered, and the maximum unambiguous range was extended compared with the single-channel systems.

# B. Small Motion Detection

To determine the performance and relative merits of the proposed 2-port monostatic transceiver front end against other systems, the implemented quadrature radar was placed 50 cm away from a mechanical actuator (Zaber T-NAOSA50) to measure the linear movements of a corner reflector, as shown in Fig. 21. The actuator was programmed to produce a 2-Hz sinusoidal movement with an amplitude of 2.5  $\mu$ m. The measurement window was set to 50 s and the selected sampling frequency was 6 kHz. The experimental results are shown in Fig. 22, where the frequency of the programmed motion was effectively detected, demonstrating the superior sensitivity of the proposed design. In addition, to assess the displacement measurement capabilities of the proposed architecture, the actuator was placed 1.5 m away from the radar and it was programmed to produce a 2-Hz sinusoidal movement with

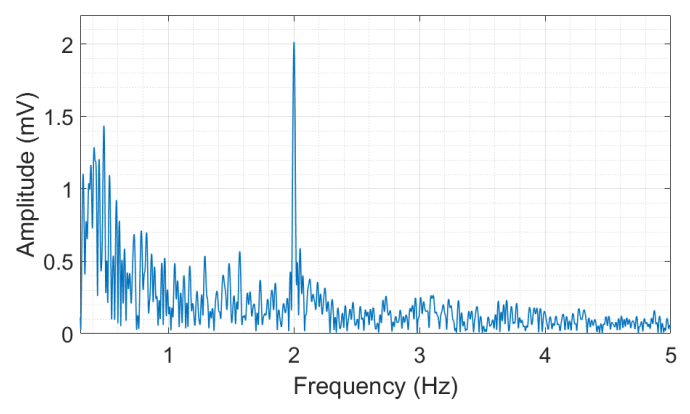


Fig. 22. Recovered spectrum for a 2-Hz sinusoidal motion with an amplitude of 2.5  $\mu$ m.

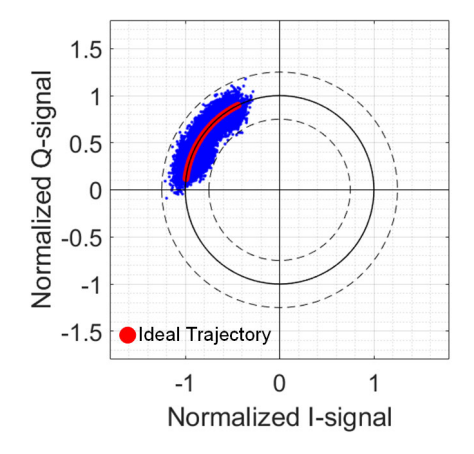


Fig. 23. Recovered constellation plot for a 2-mm sinusoidal motion.

TABLE III
PERFORMANCE COMPARISON FOR RADAR-BASED
SMALL MOTION DETECTION

	Displacement	Frequency (GHz)	A/λ (μm/m)
This work	2.5 μm	5.8	48.4
[41]	10 μm	24	800
[40]	20 μm	60	4000
[26]	95 nm	125	39.5

an amplitude of 2 mm. For this experiment, the sampling frequency was set to 250 Hz and a 40-s window was used. It should be noted that the signal-to-noise ratio (SNR) at the output of an amplifier is always worse when compared to the SNR at its input. Therefore, increasing the gain of the baseband amplifier can potentially enhance detection sensitivity if the dynamic range of the analog-to-digital converter allows. However, this will restrict the radar operation to the detection of very small motion within specific ranges, and now, the amplifier stability becomes a matter of concern. Also, a higher gain in the baseband amplifier may introduce certain challenges. Higher gain levels can lead to increased noise and the risk of signal distortion, which may impact the radar's overall performance. The recovered constellation plot is shown in Fig. 23, and a circular fitting algorithm was used to compare the recovered trajectory with the unit circle.

Moreover, simulations were carried out to compute the ideal I/Q signal generated by the programmed motion. As can be seen, the recovered displacement closely matches the ideal trajectory that fits the unitary circle, showing the low I/Q imbalance present in the proposed system. Table III shows a comparison with previously reported motion sensing radars using more complex architectures.

### V. CONCLUSION

Single- and quadrature-channel 2-port monostatic front-end architectures were proposed, designed, fabricated, and tested. The low cost, high sensitivity, and compact size inherent to these architectures make them suitable for mass deployment and collocated sensor implementation. Experiments with the implemented 5.8-GHz quadrature 2-port monostatic radar verified the high sensitivity of the proposed architecture, showing great potential for small motion sensing and human range tracking applications. Moreover, a single-channel 24-GHz 2-port radar system was designed, implemented, and tested to verify the scalability of the proposed architecture to millimeter-wave frequencies. Finally, the proposed architecture can be potentially used for millimeter-wave radar-on-chip implementation due to its low complexity and small area requirements for small wavelengths.

# REFERENCES

- [1] H. Abedi, M. Ma, J. He, J. Yu, A. Ansariyan, and G. Shaker, "Deep learning-based in-cabin monitoring and vehicle safety system using a 4-D imaging radar sensor," *IEEE Sensors J.*, vol. 23, no. 11, pp. 11296–11307, Jun. 2023.
- [2] H. Gao and C. Li, "Automated violin bowing gesture recognition using FMCW-radar and machine learning," *IEEE Sensors J.*, vol. 23, no. 9, pp. 9262–9270, May 2023.
- [3] A. Kosuge, S. Suehiro, M. Hamada, and T. Kuroda, "MmWave-YOLO: A mmWave imaging radar-based real-time multiclass object recognition system for ADAS applications," *IEEE Trans. Instrum. Meas.*, vol. 71, 2022, Art. no. 2509810.
- [4] W. Xia, Y. Li, and S. Dong, "Radar-based high-accuracy cardiac activity sensing," *IEEE Trans. Instrum. Meas.*, vol. 70, 2021, Art. no. 4003213.
- [5] A. A. Pramudita and F. Y. Suratman, "Low-power radar system for noncontact human respiration sensor," *IEEE Trans. Instrum. Meas.*, vol. 70, 2021, Art. no. 4005415.
- [6] F. Michler, B. Scheiner, T. Reissland, R. Weigel, and A. Koelpin, "Micrometer sensing with microwaves: Precise radar systems for innovative measurement applications," *IEEE J. Microw.*, vol. 1, no. 1, pp. 202–217, Jan. 2021.
- [7] C. Li, V. M. Lubecke, O. Boric-Lubecke, and J. Lin, "Sensing of life activities at the human-microwave frontier," *IEEE J. Microw.*, vol. 1, no. 1, pp. 66–78, Jan. 2021.
- [8] D. V. Q. Rodrigues, D. Zuo, Z. Tang, J. Wang, C. Gu, and C. Li, "Adaptive displacement calibration strategies for field structural health monitoring based on Doppler radars," *IEEE Trans. Instrum. Meas.*, vol. 69, no. 10, pp. 7813–7824, Oct. 2020.
- [9] K. B. Cooper et al., "A compact, low power consumption, and highly sensitive 95 GHz Doppler radar," *IEEE Sensors J.*, vol. 20, no. 11, pp. 5865–5875, Jun. 2020.
- [10] Z. Gu et al., "Blind separation of Doppler human gesture signals based on continuous-wave radar sensors," *IEEE Trans. Instrum. Meas.*, vol. 68, no. 7, pp. 2659–2661, Jul. 2019.
- [11] A. Mishra, W. McDonnell, J. Wang, D. Rodriguez, and C. Li, "Intermodulation-based nonlinear smart health sensing of human vital signs and location," *IEEE Access*, vol. 7, pp. 158284–158295, 2019.
- [12] T. Sakamoto, X. Gao, E. Yavari, A. Rahman, O. Boric-Lubecke, and V. M. Lubecke, "Hand gesture recognition using a radar echo I–Q plot and a convolutional neural network," *IEEE Sensors Lett.*, vol. 2, no. 3, pp. 1–4, Sep. 2018.

- [13] Y.-S. Su, C.-C. Chang, J.-C. Kuo, and J.-M. Kuo, "Design of self-injection-locked radar system for birds' wingbeat frequency detection," *IEEE Sensors J.*, vol. 18, no. 24, pp. 10010–10017, Dec. 2018.
- [14] H. Zhao, Z. Peng, H. Hong, X. Zhu, and C. Li, "A portable 24-GHz auditory radar for non-contact speech sensing with background noise rejection and directional discrimination," in *IEEE MTT-S Int. Microw. Symp. Dig.*, May 2016, pp. 1–4.
- [15] J.-M. Muñoz-Ferreras, Z. Peng, Y. Tang, R. Gómez-García, D. Liang, and C. Li, "Short-range Doppler-radar signatures from industrial wind turbines: Theory, simulations, and measurements," *IEEE Trans. Instrum. Meas.*, vol. 65, no. 9, pp. 2108–2119, Sep. 2016.
- [16] Á. Parra-Cerrada, V. González-Posadas, J. L. Jiménez-Martín, Á. Blanco-del-Campo, W. Hernandez, and C. Calderón-Córdova, "Low-cost measurement for a secondary mode s radar transmitter," *IEEE Trans. Instrum. Meas.*, vol. 64, no. 12, pp. 3217–3225, Dec. 2015.
- [17] J. Wang, X. Wang, L. Chen, J. Huangfu, C. Li, and L. Ran, "Noncontact distance and amplitude-independent vibration measurement based on an extended DACM algorithm," *IEEE Trans. Instrum. Meas.*, vol. 63, no. 1, pp. 145–153, Jan. 2014.
- [18] O. Said, Z. Al-Makhadmeh, and A. Tolba, "EMS: An energy management scheme for green IoT environments," *IEEE Access*, vol. 8, pp. 44983–44998, 2020.
- [19] D. Rodriguez, M. A. Saed, and C. Li, "A WPT/NFC-based sensing approach for beverage freshness detection using supervised machine learning," *IEEE Sensors J.*, vol. 21, no. 1, pp. 733–742, Jan. 2021.
- [20] C. Will, P. Vaishnav, A. Chakraborty, and A. Santra, "Human target detection, tracking, and classification using 24-GHz FMCW radar," *IEEE Sensors J.*, vol. 19, no. 17, pp. 7283–7299, Sep. 2019.
- [21] J.-M. Muñoz-Ferreras and R. Gómez-García, "A deramping-based multi-band radar sensor concept with enhanced ISAR capabilities," *IEEE Sensors J.*, vol. 13, no. 9, pp. 3361–3368, Sep. 2013.
- [22] S. Battiboia, A. Caliumi, S. Catena, E. Marazzi, and L. Masini, "Low-power X-band radar for indoor burglar alarms," *IEEE Trans. Microw. Theory Techn.*, vol. 43, no. 7, pp. 1710–1714, Jul. 1995.
- [23] D. Rodriguez and C. Li, "A low-power and low-cost monostatic radar based on a novel 2-port transceiver chain," in *Proc. IEEE Topical Conf. Wireless Sensors Sensor Netw. (WiSNeT)*, Jan. 2020, pp. 9–12.
- [24] B. Sene, D. Reiter, H. Knapp, and N. Pohl, "Design of a cost-efficient monostatic radar sensor with antenna on chip and lens in package," *IEEE Trans. Microw. Theory Techn.*, vol. 70, no. 1, pp. 502–512, Jan. 2022.
- [25] C. Li and J. Lin, "Random body movement cancellation in Doppler radar vital sign detection," *IEEE Trans. Microw. Theory Techn.*, vol. 56, no. 12, pp. 3143–3152, Dec. 2008.
- [26] D. Rodriguez and C. Li, "Sensitivity and distortion analysis of a 125-GHz interferometry radar for submicrometer motion sensing applications," *IEEE Trans. Microw. Theory Techn.*, vol. 67, no. 12, pp. 5384–5395, Dec. 2019.
- [27] J. Wang, T. Karp, J.-M. Muñoz-Ferreras, R. Gómez-García, and C. Li, "A spectrum-efficient FSK radar technology for range tracking of both moving and stationary human subjects," *IEEE Trans. Microw. Theory Techn.*, vol. 67, no. 12, pp. 5406–5416, Dec. 2019.
- [28] J. Wang, D. Rodriguez, A. Mishra, P. R. Nallabolu, T. Karp, and C. Li, "24-GHz impedance-modulated BPSK tags for range tracking and vital signs sensing of multiple targets using an FSK radar," *IEEE Trans. Microw. Theory Techn.*, vol. 69, no. 3, pp. 1817–1828, Mar. 2021.
- [29] S. Lindner, F. Barbon, S. Mann, G. Vinci, R. Weigel, and A. Koelpin, "Dual tone approach for unambiguous six-port based interferometric distance measurements," in *IEEE MTT-S Int. Microw. Symp. Dig.*, Jun. 2013, pp. 1–4.
- [30] S. Lindner, F. Barbon, S. Linz, S. Mann, R. Weigel, and A. Koelpin, "Distance measurements based on guided wave 24 GHz dual tone sixport radar," in *Proc. 11th Eur. Radar Conf.*, Oct. 2014, pp. 57–60.
- [31] D. M. Pozar, Microwave Engineering. Hoboken, NJ, USA: Wiley, 2012.
- [32] S. Franco, Design with Operational Amplifiers and Analog Integrated Circuits. New York, NY, USA: McGraw-Hill, 2001.
- [33] B. R. Phelan, K. I. Ranney, K. A. Gallagher, J. T. Clark, K. D. Sherbondy, and R. M. Narayanan, "Design of ultrawideband stepped-frequency radar for imaging of obscured targets," *IEEE Sensors J.*, vol. 17, no. 14, pp. 4435–4446, Jul. 2017.
- [34] C. Gu, Z. Peng, and C. Li, "High-precision motion detection using low-complexity Doppler radar with digital post-distortion technique," *IEEE Trans. Microw. Theory Techn.*, vol. 64, no. 3, pp. 961–971, Mar. 2016.
- [35] C. Li, J. Ling, J. Li, and J. Lin, "Accurate Doppler radar noncontact vital sign detection using the RELAX algorithm," *IEEE Trans. Instrum. Meas.*, vol. 59, no. 3, pp. 687–695, Mar. 2010.

- [36] C. Gu, C. Li, J. Lin, J. Long, J. Huangfu, and L. Ran, "Instrument-based noncontact Doppler radar vital sign detection system using heterodyne digital quadrature demodulation architecture," *IEEE Trans. Instrum. Meas.*, vol. 59, no. 6, pp. 1580–1588, Jun. 2010.
- [37] R. Zetik, J. Sachs, and R. Thoma, "UWB short-range radar sensing— The architecture of a baseband, pseudo-noise UWB radar sensor," *IEEE Instrum. Meas. Mag.*, vol. 10, no. 2, pp. 39–45, Apr. 2007.
- [38] Y. Li et al., "An X-band multifrequency difference frequency-shift keying CMOS radar for range tracking and AI-based human gesture recognition," *IEEE Sensors J.*, vol. 23, no. 11, pp. 11600–11614, Jun. 2023.
- [39] J. Wang, D. Nolte, K. Tanja, J.-M. Muñoz-Ferreras, R. Gómez-García, and C. Li, "Trade-off on detection range and channel usage for moving target tracking using FSK radar," in *Proc. IEEE Topical Conf. Wireless Sensors Sensor Netw. (WiSNeT)*, Jan. 2020, pp. 38–41.
- [40] T.-Y.-J. Kao, A. Y.-K. Chen, Y. Yan, T.-M. Shen, and J. Lin, "A flip-chip-packaged and fully integrated 60 GHz CMOS micro-radar sensor for heartbeat and mechanical vibration detections," in *Proc. IEEE Radio Freq. Integr. Circuits Symp.*, Jun. 2012, pp. 443–446.
- [41] F. Barbon, G. Vinci, S. Lindner, R. Weigel, and A. Koelpin, "A six-port interferometer based micrometer-accuracy displacement and vibration measurement radar," in *IEEE MTT-S Int. Microw. Symp. Dig.*, Jun. 2012, pp. 1–3.



Ashish Mishra (Member, IEEE) received the B.E. degree in electronics and telecommunication engineering from the University of Mumbai, Mumbai, India, and the M.S. and Ph.D. degrees in electrical engineering from Texas Tech University, Lubbock, TX, USA, in 2016 and 2020, respectively.

From February 2020 to August 2020, he was working as an Intern at Unknot ID, Orlando, FL, USA, utilizing mobile phones as sonar devices for human vital signs and gesture monitoring.

From December 2020 to May 2021, he worked as a Postdoctoral Research Associate with Northeastern University, Boston, MA, USA, and a Hardware Engineer with Oculii Corporation, Dayton, OH, USA, from May 2021 to January 2022. He has been working as a Radar Signal Processing Engineer at Magna International, Cambridge, MA, USA (formerly Veoneer US, LLC) since January 2022. His current research interests include microwave circuits, wireless RF sensors, and their use in automotive and biomedical applications.

Dr. Mishra is a reviewer of Nature (Springer), IEEE TRANSACTIONS ON MICROWAVE THEORY AND TECHNIQUES, IEEE MICROWAVE AND WIRELESS COMPONENTS LETTERS, and IEEE ACCESS.



**Daniel Rodriguez** (Member, IEEE) received the B.S. degree in electronics and telecommunication engineering from the Universidad Autonoma del Caribe, Barranquilla, Colombia, in 2014, and the Ph.D. degree in electrical engineering from Texas Tech University, Lubbock, TX, USA, in 2022.

He is currently an Analog Design Engineer at Intel Corporation, Hillsboro, OR, USA. His research interests include radar systems, microwave/millimeter-wave sensing, and

microwave circuits.

Dr. Rodriguez was awarded as an HSF Scholar in 2019. He received the IEEE MTT-S Graduate Fellowship Award in 2020 and the JT and Margaret Talkington Graduate Fellowship in 2017. He is an active reviewer of the IEEE TRANSACTIONS ON MICROWAVE THEORY AND TECHNIQUES, the IEEE JOURNAL OF ELECTROMAGNETICS, RF AND MICROWAVES IN MEDICINE AND BIOLOGY, and the IEEE SENSORS JOURNAL.



Davi V. Q. Rodrigues (Member, IEEE) received the B.S. degree in communications engineering from the Military Institute of Engineering, Rio de Janeiro, Brazil, in 2017, and the Ph.D. degree in electrical engineering from Texas Tech University, Lubbock, TX, USA, in 2023.

He is an Assistant Professor at the University of Texas at El Paso, El Paso, TX. Prior to academia, Dr. Rodrigues served first with the Brazilian Navy and later with the Brazilian Army, where he was commissioned as First

Lieutenant. He joined Texas Tech University as a Research Assistant in the fall of 2018. In the summer of 2021, he was with Uhnder, Inc., Austin, TX, where he was involved in the design and evaluation of signal processing algorithms for mitigation of radar interference. In the spring and summer of 2022, he was with Abbott Laboratories, Los Angeles, CA, USA, where he worked on the design of antennas and microwave systems for implantable medical devices. In the fall of 2022, he conducted research on wireless networks assisted by intelligent reflective surfaces at the Advanced Wireless Research and Development Group, Global Office of the CTO, Dell Technologies, Ottawa, ON, Canada. His current research interests include signal processing for radar and communication systems, wireless sensors for smart living and biomedical applications, and microwave/millimeter-wave circuits.

Dr. Rodrigues was a recipient of the IEEE MTT-S Tom Brazil Graduate Fellowship Award, the Texas Tech Horn Distinguished Professors Graduate Achievement Award, and the University of Texas System Rising STARs Award.



Mohammad A. Saed (Senior Member, IEEE) received the B.S. degree in electrical engineering from Middle East Technical University, Ankara, Turkey, in 1983, and the M.S. and Ph.D. degrees in electrical engineering from Virginia Tech, Blacksburg, Blacksburg, VA, USA, in 1984 and 1987, respectively.

From 1989 to 1990, he was a Postdoctoral Research Associate at Virginia Tech. In 1990, he joined the Faculty of the Electrical Engineering Department, State University of New York,

New Paltz, NY, USA. In 2001, he joined the Electrical and Computer Engineering Department, Texas Tech University, Lubbock, TX, USA, where he is currently an Associate Professor. His research interests include applied electromagnetics with an emphasis on RF/microwave applications in imaging, sensing, and manufacturing; computational electromagnetics; antennas; and microwave components.



Changzhi Li (Senior Member, IEEE) received the Ph.D. degree in electrical engineering from the University of Florida, Gainesville, FL, USA, in 2009.

He is a Professor at Texas Tech University, Lubbock, TX, USA. His research interests include microwave/millimeter-wave sensing for healthcare, security, energy efficiency, structural monitoring, and human-machine interface.

Dr. Li is a Fellow of the National Academy of Inventors (NAI). Dr. Li is an IEEE Microwave

Theory and Techniques Society (MTT-S) Distinguished Microwave Lecturer in the Tatsuo Itoh class of 2022–2024. He was a recipient of the IEEE Sensors Council Early Career Technical Achievement Award and the ASEE Frederick Emmons Terman Award. He is an Associate Editor of the IEEE JOURNAL OF ELECTROMAGNETICS, RF AND MICROWAVES IN MEDICINE AND BIOLOGY.